Full Length Article

Air- and water-stable halide perovskite nanocrystals protected with nearly-monolayer carbon nitride for CO_2 photoreduction and water splitting

Devika Laishram [a,b], Sheng Zeng [a], Kazi M. Alam [a,d], Aarat P. Kalra [a,c], Kai Cui [d], Pawan Kumar [a,e,*], Rakesh K. Sharma [b,*], Karthik Shankar [a,*]

[a] Department of Electrical and Computer Engineering, University of Alberta, 9211 - 116 St, Edmonton, Alberta T6G 1H9, Canada
[b] Department of Chemistry, Indian Institute of Technology Jodhpur, Jodhpur, Rajasthan 34201, India
[c] Department of Physics, Faculty of Science, 4-181 CCIS, University of Alberta, Edmonton T6G 2E1, Canada
[d] Nanotechnology Research Centre, National Research Council of Canada, Edmonton T6G 2M9, Canada
[e] Department of Chemical and Petroleum Engineering, University of Calgary, 2500 University Dr. NW, Calgary, Alberta T2N 1N4, Canada

ABSTRACT

Halide perovskites are exciting candidates for broad-spectrum photocatalysts but have the problem of ambient stability. Protective shells of oxides and polymers around halide perovskite nano- and micro-crystals provide a measure of chemical and photochemical resilience but the photocatalytic performance of perovskites is compromised due to low electron mobility in amorphous oxide or polymer shells and rapid charge carrier recombination on the surface. Herein an *in situ* surface passivation and stabilization of $CsPbBr_3$ nanocrystals was achieved using monolayered graphenic carbon nitride (CNM). Extensive characterization of carbon nitride protected $CsPbBr_3$ nanocrystals (CNMBr) indicated spherical $CsPbBr_3$ nanoparticles encased in a few nm thick g-C_3N_4 sheets facilitating better charge separation *via* percolation/tunneling of charges on conductive 2D nanosheets. The CNMBr core-shell nanocrystals demonstrated enhanced photoelectrochemical water splitting performance and photocurrent reaching up to 1.55 mA cm^{-2}. The CNMBr catalyst was successfully deployed for CO_2 photoreduction giving carbon monoxide and methane as the reaction products.

1. Introduction

Nature has its own cycle to curb the rising CO_2 level by means of photosynthesis and mineralization processes [1,2]. However, due to unchecked exploitation of non-renewable fossil fuels and deforestation, the atmospheric CO_2 level has ascended to levels (416 ppm in 2020) that need immediate measures to mitigate drastic environmental and climate impacts [3–5]. Consequently, the inexhaustible solar energy resource is being increasingly viewed as a means to supplant the planet's reliance on fossil fuels. Therefore, solar energy harvesting through processes such as photocatalytic CO_2 reduction to hydrocarbon fuels, photo-electrochemical electrolyzers, photocatalytic hydrogen generation through water-splitting and photovoltaic electricity generation are the focus of intense research attention [6,7]. Of all the aforementioned technologies, photovoltaics is the most mature and economically viable, and yet suffers from certain shortcomings such as intermittency, long

energy payback times and expensive grid storage [8]. Thermochemical approaches such as the Fischer-Tropsch process use catalyst, active substrate (i.e. hydrogen) and heat to transform stable CO_2 ($\Delta_{Hf} = -394$ kJ/mol) into valuable chemicals such as hydrocarbons, ethylene glycol, ethylene carbonates etc [9,10]. However, the energy intensive nature and use of expensive catalysts make these processes unfavorable.

Photoelectrochemical water splitting to produce clean hydrogen and photocatalytic conversion of CO_2 to form reduced compounds such as CO, methane, methanol, *etc* offers a potential solution to meet at least a portion of global energy demand due to their reliance on widely available sunlight, water and CO_2 [11–16]. Hydrogen has a high energy density and offers a means for storing energy and transporting it to the point of demand [17]. CO_2 reduction produces hydrocarbon fuels such as methane, ethane, methanol, etc which are even more compatible than hydrogen with the existing energy production and distribution infrastructure, thus requiring less capital investment to switch from fossil

fuels to solar fuels [18].

Over the past decade, numerous nanostructured semiconductors including inorganic, organic and organic/inorganic hybrid materials have been engineered to convert water into hydrogen and CO_2 into hydrocarbons [19–23]. However, the lack of stable, efficient, and inexpensive photocatalysts and photoelectrodes with broad visible absorption and long-lived charged carriers remains a challenge for the successful deployment of technology that can compete with fossil fuels. Quantum dots of hybrid organic-inorganic halide perovskites such as $CH_3NH_3PbI_3$, have generated enormous research interest for use in photovoltaics and photocatalysis but suffer from low ambient stability imposing challenges in fabrication and device operations [24–27]. The narrow bandgap, intense absorption coefficient and long carrier diffusion lengths in halide perovskites are particularly attractive for solar energy harvesting applications. When the hygroscopic organic cation in $MAPbI_3$ is replaced by Cs^+, the 'all inorganic' halide perovskite $CsPbX_3$ results, with comparable optoelectronic properties but superior stability (up to three months in dry air) [28–32]. However, due to its inherent ionic nature, it still shows instability in water. Therefore, to overcome this drawback certain strategies have been adopted such as the formation of nanocomposites with more durable materials or passivation by a layer of either semiconductor or dielectric [32–36]. Nevertheless, these strategies become ineffective due to reduced charge transport through the passivating layer and loss of surface ligands during post-processing such as washing/rinsing and isolation from the reaction mixture [37].

To address the challenges of processing $CsPbBr_3$ perovskites in aqueous and other polar solvents, graphene-like materials have been introduced. Graphene oxide (GO) and reduced graphene oxide (rGO) have been used to passivate the surface of $CsPbBr_3$/$CH_3NH_3PbI_3$ which behave as electron shuttles to increase the performance in CO_2 reduction and sunlight-driven water splitting respectively [38,39]. However, the stability of these hybrids in water is uncertain. Furthermore, the simultaneous efficient extraction of photogenerated electrons and holes is rather difficult because built-in electric fields at the core-shell interface regardless of sign will direct one type of carrier towards the core (a potential dead-end). Additionally, scalable production of graphene/graphene oxide is costly and uses toxic chemicals which introduces secondary contaminants in the environment. Metal-free 2D graphenic frameworks composed of earth-abundant elements such as C and N have been identified as promising photocatalytic materials due to the multitude of exposed active sites, conjugated backbones, low charge transfer resistance and wide solar light response up to near-infrared (NIR) wavelengths [40–42]. Graphitic carbon nitride (g-C_3N_4, CN), a moderate band gap (2.7 eV) polymeric semiconductor, is well-suited for solar fuel generation due to favorable band positions (E_{CB}: −1.1 and E_{VB}: + 1.6 eV *vs* NHE) [43–47]. g-C_3N_4 can be manufactured at industrial scale (in tonnes) using cheap precursors such as urea, thiourea and melamine. Bulk carbon nitride is not ideal as a passivating shell for $CsPbBr_3$ quantum dots due to multilayer π-π stacking and intersheets hydrogen bonding which acts as localized recombination centers and hinders the free movement of charge carriers [48]. Distinct from previous approaches which were limited to mixing of $CsPbBr_3$ quantum dots with bulk carbon nitride [49], we have developed an exclusive *in situ* protocol to passivate as well as wrap the $CsPbBr_3$ nanocrystals with periodic CNM sheets. Passivation of $CsPbBr_3$ nanocrystals with conjugated CN sheets minimizes grain boundary recombination due to superior crystallization as demonstrated by us and others [50,51]. The tunneling of photogenerated holes in the $CsPbBr_3$ core through few nm thick CN sheets, better charge carrier mobility in periodic/crystalline conjugated CN sheets and the presence of ample basic sites with a selective affinity toward CO_2 enhance the photocatalytic performance [52,53]. Additionally, selective permeability of CN sheets for protons and hydrogen over H_2O, N_2, CO_2 and O_2 protects the $CsPbBr_3$ core and facilitates selective percolation of protons on the surface of perovskite to extract electrons followed by desorption of reduced hydrogen [54–56].

2. Materials and methods

2.1. Reagents and materials

Lead bromide (PbBr$_2$, 98 + %), cesium carbonate (Cs$_2$CO$_3$, 99.5 % purity) and 1-Octadecene (ODE, 90 %) were procured from Acros Organics. Analytical grade oleylamine (OAm, 70%), dicyandiamide (99%), anhydrous Na$_2$SO$_4$ (99%), titanium di-isopropoxide (97%), acetic acid (≥99.85%) and formaldehyde (37%) were obtained from Sigma Aldrich. Hexane, oleic acid (OA) HNO$_3$ and HCl (37%) were procured from Fischer Scientific. No further purification was employed, and all the chemicals were used as received. The solvents used were of HPLC grade and DI water was used throughout the study. Fluorine-doped tin oxide (FTO) coated glass slides were purchased from Hartford Tec Glass Company (specifications: TEC 7, resistivity: 6–8 O/square, visible transmittance: 80–82 %, haze: 5%). The surface of FTO was cleaned/degreased from organic-inorganic impurities by ultrasonication in acetone, methanol and water respectively for 10 min each. $^{12}CO_2$ (99% purity) was obtained from Praxair (Canada) while isotopically labeled $^{13}CO_2$ (99% purity) was obtained from Cambridge Isotope Laboratories, Inc. (USA).

2.2. Synthesis of CsPbBr3 nanocrystals

Step 1. Preparation of Cesium Oleate (CsOL): Cesium oleate precursor was synthesized by mixing 36 wt% Cs$_2$CO$_3$/OA in 1-octadecene. The reaction mixture was heated in a three-neck bottom flask under an inert atmosphere at 120 °C for 1 h and later increased to 150 °C until complete dissolution of Cs$_2$CO$_3$ precursor. Typically, 814 mg of Cs$_2$CO$_3$, 2.5 mL OA and 10 mL ODE were mixed to form Cs-oleate solution which was stored at room temperature and used when needed by re-heating at 150 °C.

Step 2. Synthesis of CsPbBr$_3$ Nanocrystals: A typical hot injection method was adopted for the synthesis of CsPbBr$_3$ nanocrystals under an inert N$_2$ atmosphere in a glovebox [33,57]. A two-neck flask containing 138 mg PbBr$_2$ in 10 mL ODE was heated at 120 °C for 1 h under continuous stirring. Subsequently, 1 mL each of OA and OAm were injected in the reaction system followed by increasing the temperature to 180 °C. To this solution, 1 mL of the Cs-oleate solution was injected rapidly after which the solution turned turbid and acquired a fluorescent green color. After 5 s of the reaction, the system was rapidly cooled using an ice water bath. The obtained solid was dissolved in hexane and washed with hexane three times in a centrifuge at 8000 rpm. The collected precipitate was kept in a hexane suspension for further use.

2.3. Synthesis of bulk graphitic carbon nitride, g-C$_3$N$_4$, CN

High temperature thermal polycondensation polymerizations of dicyandiamide under a semi-closed environment give bulk graphitic carbon nitride [58,59]. Briefly, in a silica crucible, 5 g dicyandiamide was taken and covered loosely with a lid followed by heating at 550 °C with a heating rate of 8 °C min^{-1} up to 300 °C and 2 °C min^{-1} up to 550 °C and finally holding the temperature 550 °C for 4 h. The afforded bulk pale yellow powder finely ground and used for further experiments.

2.4. Synthesis of monolayer carbon nitride sheets nanocomposite (CNM)

The nearly monolayer-thick carbon nitride sheets were synthesized by following a previously reported protocol with slight modifications [60]. In brief, a 50 mL round bottom (RB) flask with a magnetic stirrer was placed in an ice bath. The RB flask was charged with 0.5 g CN powder followed by slow addition of 50 mL conc. HNO$_3$ (65 wt%) and stirred for 15 min. The ice bath was removed, and the obtained suspension was refluxed at 80 °C for 3 h (**Caution:** maintain the heating temperature below 100 °C). The solution turned turbid and milky white indicating successful chemical exfoliation of CN sheets. The obtained sol

was diluted with DI water, centrifuged and washed several times with water until the pH became neutral. The obtained monolayer sheets (CNM) were dispersed in methanol by sonication for further use. The concentration of sheets in mg/mL was determined by drying a certain amount of solution and calculating the dry weight of the sample.

2.5. Synthesis of monolayer carbon nitride protected $CsPbBr_3$ nanocrystals (CNMBr)

The carbon nitride protected $CsPbBr_3$ nanocrystals (CNMBr) were prepared by an *in situ* approach. Firstly, 5 mL of CNM in methanol was centrifuged and washed with hexane to remove residual methanol. The obtained CN sheets were dispersed in 2 mL ODE using sonication. The ODE dispersed CN sheets were added to 8 mL of $PbBr_2$ in ODE solution and heated at 120 °C for 1 h under continuous stirring under N_2 atmosphere. The rest of the steps were identical to the synthesis of $CsPbBr_3$ nanocrystals except that the mixture was stirred for 15 min after the addition of CsOL. After washing with hexane, the solid was dispersed and used later to evaluate photocatalytic performance. The obtained nanoparticles were stable in water and other polar solvents and remained fluorescent for 2 months in the air.

For comparison, we also prepared $CsPbBr_3$ enwrapped CNM particles by the post-synthesis approach. In short, 5 mL of CNM in methanol was centrifuge, washed with hexane and re-dispersed in 2 mL of hexane using sonication. Note that due to hydrophobic nature, CN sheets are poorly dispersible in hexane and require sonication before use. The obtained solution was rapidly added to the suspension of $CsPbBr_3$ nanocrystals in hexane and sonicated for 5 min followed by stirring for 2 h. Finally, the nanoparticles were separated by centrifugation and re-dispersed in hexane. The $CsPbBr_3$/CNM nanoparticles obtained by the post-synthesis approach immediately get deactivated in polar solvents.

2.6. Photo-/electrochemical measurements

2.6.1. Electrochemical characterization

The electrochemical properties of materials were investigated using a CHI660E series electrochemical workstation in a three-electrode setup. The working electrode (anode) was prepared by drop-casting materials on TiO_2 blocking layer coated FTO glass followed by drying the solvent [61,62]. For the preparation of CN/CNM photoanode, a calculated amount to CNM/CN was mixed with isopropanol and α-terpineol mixture, followed by sonication. The obtained suspension was drop cast on the seed blocking layer containing FTO glass and heated to dry the solvent. The obtained electrode was covered with a Surlyn film with a small window. The CNMBr electrode was prepared by directly drop-casting a calculated amount of hexane dispersed materials on FTO glass followed by coverage with Surlyn window.

Platinum was used as the counter electrode (cathode) while Ag/AgCl electrode was used as the reference electrode. The electrolyte used was 0.5 M Na_2SO_4. Mott-Schottky plot to determined flat band potential (V_{fb}) and carrier density was derived from impedance-potential measurement in 0.5 M Na_2SO_4 by sweeping the applied bias in the range of –1.0 to + 1.0 V (*vs* Ag/AgCl) at a frequency of 1 kHz. Nyquist plots were obtained through electrochemical impedance spectroscopy (EIS) to determine the semiconductor-electrolyte interaction under dark and AM1.5 G solar irradiation. EIS was performed using a three-electrode configuration at an applied bias of –0.5 V *vs* Ag/AgCl in 0.1 M Na_2SO_4, with an AC amplitude of 5 mV at a frequency of 100 kHz. To carry out measurements under light irradiation AM1.5G one sun illumination from a Class A Newport Oriel solar simulator with a power density of 100 mW cm^{-2} at the surface of samples was used. The fitting of Nyquist data was performed in CHI660E software to extract an equivalent circuit.

2.6.2. Photoelectrochemical water splitting

The photoelectrochemical water splitting performance of the samples was determined in a three-electrode configuration using materials deposited on TiO_2 coated FTO as photoanode while Pt and Ag/AgCl served as a cathode (counter electrode) and reference electrode respectively. All the measurements were performed in 0.1 M Na_2SO_4 electrolyte. The photocurrent response of materials was determined by linear sweep voltammetry (LSV) to measure photocurrent density (*J*) as a function of applied bias. The applied bias was swept in the range −0.8 to + 1.0 V *vs* Ag/AgCl at a 0.1 mV scan rate. The photocurrent density was measured under AM1.5 G simulated solar light with/without filter and in dark conditions. The light response and long-term resiliency of materials under the photoirradiation conditions were determined by measuring the photocurrent density as a function of time (*i-t* curve) during light On-Off cycles at constant water oxidation potential (+0.6 V *vs* Ag/AgCl). Additionally, to analyze the spectral dependence of the photocurrent, samples were irradiated with monochromatic 420, 460, 520, 580, 640, 740 and 840 nm wavelength LEDs by maintaining a power density of 21.1 mW cm^{-2} at the surface of the sample.

2.7. Gas phase CO_2 reduction experiment

The photocatalytic CO_2 reduction experiment was carried out in a cylindrical reactor (30 mL internal volume) with a quartz window, as mentioned in our previous reports [63,64]. Firstly, the samples were deposited on a 1 cm^{-2} area of a glass slide by five successive spin coating steps at 3000 rpm followed by drying. The obtained samples were placed in the reactor and 200 μL DI water was added around the sample in the reactor. The reactor was purged several times with nitrogen to remove any trace of atmospheric gas followed by purging with CO_2 and finally, a 50-psi pressure of CO_2 was maintained in the reactor. The reactor was heated to 80 °C to evaporate the water and saturate the chamber with water vapor. The photocatalytic CO_2 reduction performance was evaluated by irradiating the photoreactor under AM1.5 G one sun simulated sunlight for 2 h while maintaining a power density of 100 mW cm^{-2} on the sample's surface. After the reaction, the gaseous products were analyzed using a Shimadzu gas chromatograph equipped with a Porapak Q column, and a molecular sieve column, and a pulsed discharge detector (PDD) under the following conditions: He carrier flow rate of 0.5 mL min^{-1}, detector temperature of 160 °C, and oven temperature - started from 60 °C and raised to 160 °C to expel water vapor. A calibration gas mixture supplied from Sigma was used for the quantification of reaction products. To validate that the CO_2 reduction products were truly generated because of CO_2 photoreduction and not because of the degradation of organics/contamination, control experiments (sanity tests) were performed by excluding one component under identical conditions 1) Under dark; 2) Using N_2 instead of CO_2; 3) Without catalyst under AM1.5G one sun illumination. Isotope labeling experiments using $^{13}CO_2$ instead of $^{12}CO_2$ were carried out under identical conditions to prove that the CO_2 reduction was truly photocatalytic. Gas chromatography-mass spectrometry (GC–MS) was employed to analyze products of $^{13}CO_2$ reduction and verify that the products were from photocatalytic transformation. Additional information on physico-chemical characterization of samples is provided in Supplementary Information.

3. Results and discussion

3.1. Structure, morphology and composition of halide perovskite colloidal nanoparticles, carbon nitride nanosheets, and $CsPbBr_3$@CNM core-shell nanoparticles

Pristine cesium lead bromide, $CsPbBr_3$ perovskite nanocrystals were synthesized by hot injection method using $PbBr_2$ and cesium oleate ($C_{18}H_{33}O_2Cs$, CsOL) as precursors, and 1-octadecene (ODE) as a solvent while oleylamine (OAm) and oleic acid (OA) were used as binary ligand system to sterically stabilize the products [33,57]. Fig. 1 provides a schematic illustration of the synthesis protocol. The reaction of $PbBr_2$ dispersed in high boiling solvent/ligands with CsOL followed by
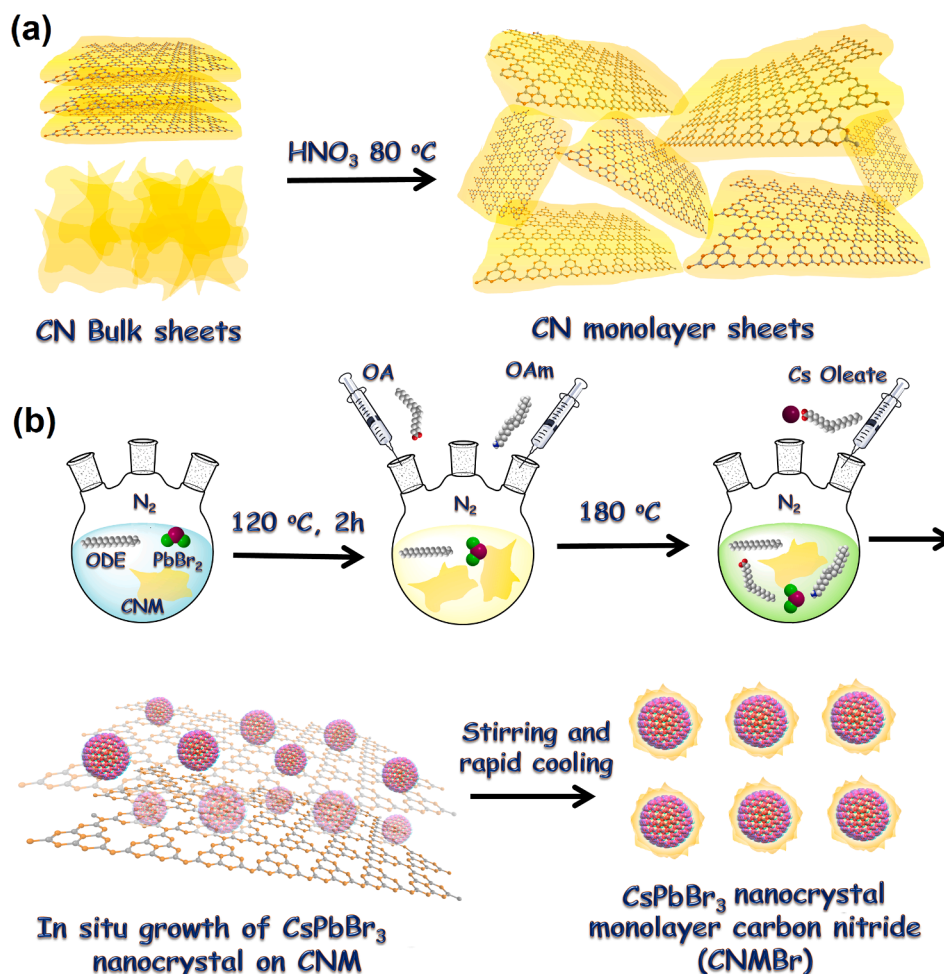
Fig. 1. Synthetic protocol for (a) CN monolayer graphenic sheets (b) *in situ* synthesis of CNMBr using CsPbBr$_3$ and CNM.

instantaneous quenching in an ice bath leads to the formation of the CsPbBr$_3$ nanocrystals. The OA protonates OAm in a nonpolar solvent and oleylammonium promotes the growth of CsPbBr$_3$ nanocrystals [65,66]. The CsPbBr$_3$ nanocrystals were purified by centrifugation and washing with hexane and finally dispersed in hexane. Bulk graphitic carbon nitride, g-C$_3$N$_4$ (CN) constituted of tris-s-triazine (heptazine, C$_6$N$_7$) moieties linked together with tertiary nitrogen was synthesized by condensation polymerization of dicyandiamide at elevated temperature (550 °C) [58,67]. The condensation polymerization of dicyandiamide proceeds *via* melamine, melam and melem intermediates that finally forms graphitic carbon nitride (CN) (see Supporting Information for synthesis details). The π-stacked and interlayer hydrogen-bonded sheets of bulk carbon nitride were transformed into nearly monolayered carbon nitride sheets (CNM) *via* HNO$_3$ assisted exfoliation at 80 °C (Fig. 1a) [60]. Treatment of CN sheets with strong HNO$_3$ at high temperature protonates nitrogens and strand nitrogens (NH/NH$_2$) in stacked carbon nitride sheets to form ammonium type local substructure [68,69]. Due to the intercalation of protons in between layered CN sheets and attachment with stranded nitrogen atoms *via* Brønsted acid/base interaction, the intersheets hydrogen bonding is broken leading to exfoliation of sheets [70,71]. The strong oxidizing nitrate ions (NO$_3^-$) fractionally oxidize CN sheets and ionic repulsion in-between sheets further facilitate their exfoliation and separation. The resulting sol containing CN monolayer sheets (CNM) suspended in HNO$_3$ were diluted with water and centrifuged followed by washing with water until pH-7 was reached. Then CNM were dispersed in methanol, centrifuged and washed with hexane to remove residual methanol and finally dispersed in ODE for further use. The CNM protected CsPbBr$_3$ nanocrystals (CNMBr) were

synthesized by *in situ* approach using ODE dispersed CNM and PbBr$_2$ followed by heating and addition of OAm, OA and CsOL (Fig. 1b). The resulting CNMBr was stirred for 15 min prior to quenching of resulting solution in an ice bath, to achieve better surface coverage with CN. The resulting CNMBr core-shell quantum dots were washed with hexane and dispersed in hexane for further use. The samples displayed excellent green photoluminesence under UV excitation as will be discussed later (also see Fig. S5 in Supporting Information). The average diameter of pristine CsPbBr$_3$ quantum dots in hexane was found to be 24 nm as measured by dynamic light scattering (DLS) (Fig. S8 in Supporting Information). The obtained average diameter value was slightly larger than the reported value (18 nm) [33] because DLS measures the hydrodynamic radius of the particle, which was increased because of the presence of long alkyl chain ligands on the surface of CsPbBr$_3$. The value of average particle size for CNMBr samples was found to be 122 nm suggesting encasing of multiple perovskite particles in the CNM scaffold (Fig. S8).

The surface morphologies of CNM and CNMBr samples were determined using electron microscopy (Fig. 2 and Fig. S1-S3 in Supporting Information). The SEM micrograph of CNM on the TEM grid displayed crumpled and agglomerated graphene-like sheets showing few-layered features at the edge (Fig. S1). The monolayer CNM sheets tend to agglomerate in solvent due to intersheet hydrogen bonding. The SEM image of CNMBr deposited on FTO showed monodispersed spherical CsPbBr$_3$ nanoparticles with an average diameter of 20 nm embedded in a CNM matrix (Fig. 2a-c and Fig. S2a-c in Supporting Information). The FESEM EDX mapping clearly demonstrates the presence of all the constituent elements (Cs, Pb, Br, C and N) with a high density of spot-on
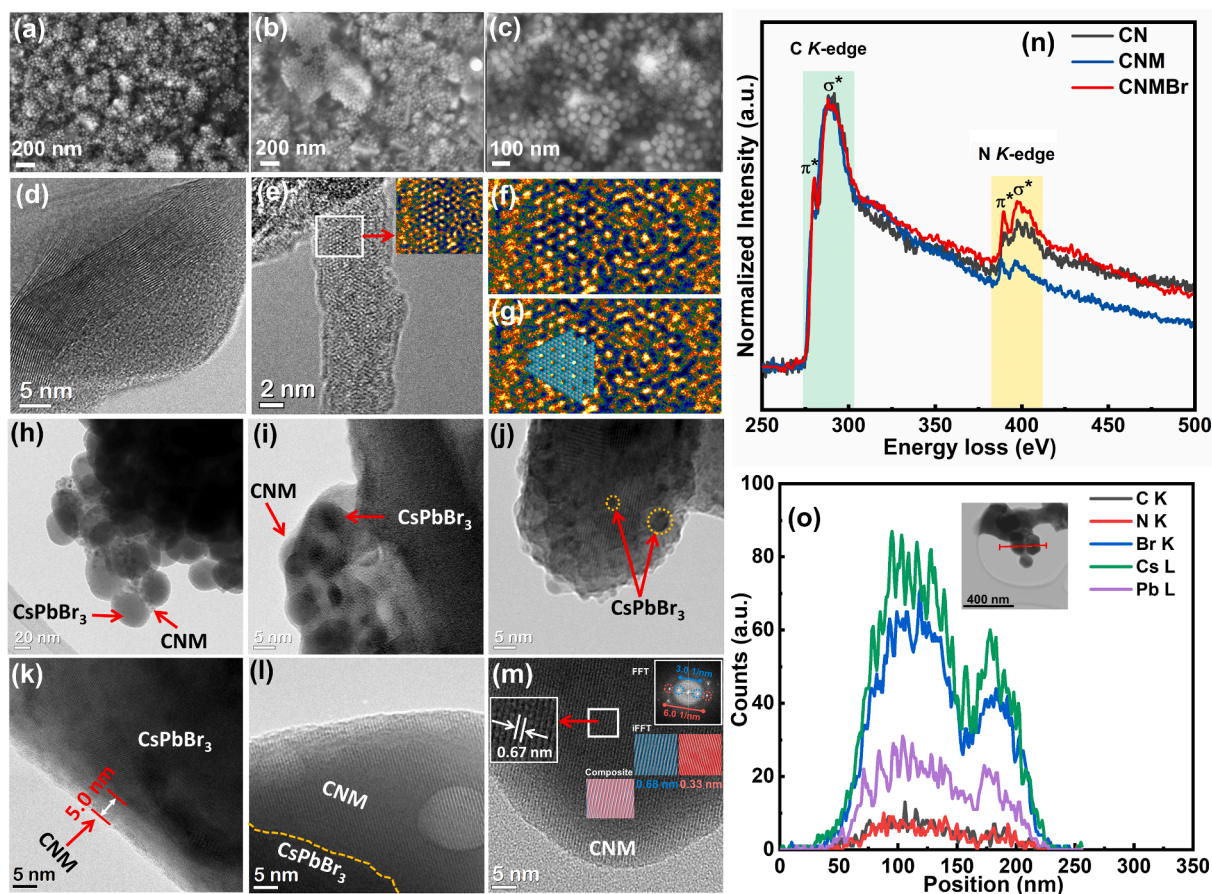
Fig. 2. (a-c) FE-SEM image of CNMBr; HR-TEM image of CNM at (d) 5 nm scale bar showing lattice fringes and stacking patterns of the sheets, (e) 2 nm scale bar showing lattice fringes and atomic dots and inset showing the magnified color view of the selected region (f) Enlarged region of the color map showing the distribution of heptazine unit dots (g) Trigonal planar tris-*s*-triazine (heptazine) units of carbon nitride superimposed on atomic dots showing the presence of heptazine unit in CNM, low resolution TEM images of CNMBr at (h) 20 nm, (i) 5 nm and (j) 5 nm scale bar showing $CsPbBr_3$ nanocrystals and their distribution in CNMBr composite; HR-TEM images of CNMBr at (k-m) 5 nm scale bar showing $CsPbB_3$ enwrapped CNM sheets nanohybrid (s) 5 nm scale bar showing lattice fringes, **Inset:** left inset; Moire fringe, right upper; FFT of image, lower inset panel: iFFT of FFT image showing two crystalline planes with 0.68 nm (blue) and 0.33 nm (red) *d*-spacing corresponding to Moire fringe and interplanar distance of stacked CNM sheets respectively; Middle inset composite of two images superimposed on the lattice plane of the TEM image. (n) Inner shell ionization edge (core loss) electron energy loss spectra (EELS) of CN (black), CNM (blue), CNMBr (red) showing the contribution of σ* and π* signals in C *K*-edge and N *K*-edge energy loss; (o) STEM EDX line scan of CNMBr particles showing the distribution of C, N, Br, Cs and Pb along the line.

nanoparticle features (Fig. S2d-l and Figure S3a-f). EDX spectra show the presence of all the elements in the CNMBr (Fig. S2j and Fig. S3g). However, the relative intensity of nitrogen remains low which might be due to the obscuring of signals from the diffraction of high-density elements. Further, SEM elemental mapping of CNMBr samples on the TEM grid displayed the uniform distribution of all the elements in the nanoparticle morphology (Fig. S4 in Supporting Information). The ultrafine morphological attributes of materials were determined using high-resolution transmission electron microscopy (HR-TEM) (Fig. 2d-m and Fig. S5 in Supporting Information). The HR-TEM images of CNM at a 5 nm scale bar show the nanoporous structure and well-ordered stacked carbon nitride nanosheets. The CN sheets separated by breaking H bonding between stand NH/NH_2 tend to re-stack after removal of strong acidic solvent HNO_3, which increases crystallinity (Fig. 2d) [71–74]. Another TEM image displayed several periodic low-density spots arising from the periodic arrangement of heptazine units (Fig. 2e). Color mapping of the magnified area clearly shows the hexagonal arrangement of the spots [75,76]. The space-filling modal of carbon nitride sheets demonstrates that tertiary N-linked heptazine units are perfectly superimposed on the high density spots while bright low density spots are visible from the in-plane interstitial cavities (Fig. 2f and g). These verify the presence of a periodic arrangement of heptazine units in the

CN network.

The HR-TEM image of CNMBr shows spherical $CsPbBr_3$ nanoparticles with 20–25 nm sizes glued together with carbon nitride (Fig. 2h). HR-TEM images collected in another region of samples show $CsPbBr_3$ nanoparticles enwrapped in CNM matrix (Fig. 2i). It can be seen from Fig. 2j that the diameter of a few nanoparticles distributed in the CNM matrix was in the 5–10 nm range which shows that instantaneous *in situ* growth of $CsPbBr_3$ in CN matrix changes the size distribution. The HR-TEM image of CNMBr at 5 nm scale bar in Fig. 2k, clearly shows dense $CsPbBr_3$ coated with approximately 5 nm thick low-density carbon nitrides. As expected, the thickness of CNM on $CsPbBr_3$ nanocrystals varies at different sample spots. The Moire fringes with 0.67 nm spacing of carbon nitride originating from superimposing stacked disordered sheets are clearly visible in the shell structure (Fig. 2l and m) [77]. The FFT of TEM images shows two bright spots suggesting the presence of two lattice planes in the sheets. The iFFT of FFT images clearly show two crystalline planes with 0.33 nm and 0.68 nm d-spacing corresponding to the interplanar distance of carbon nitride sheets and Moire fringes (mismatched superimposition) (Fig. 2m) respectively. The composite iFFT image of both planes superimposed on TEM images reveals that 0.33 nm planes corresponding to interplanar stacking [78,79] were merged with large spacing Moire fringes and images seem to dominate

via only one plane (Fig. 2m). Additionally, HR-TEM images at low and high magnification are provided in Fig. S5 in Supporting Information.

The nature of C/N bonding and electronic state of the CN material in CN, CNM and CNMBr was determined by electron energy loss spectroscopy (EELS) through measurement of the C *K*-edges and N *K*-edges energy loss (Fig. 2n). EELS spectra of CN, CNM and CNMBr displayed two major peaks originating from C-*K* and N-*K* edge energy loss [80]. The C *K*-edges constituted of two peak components centered at 283.4 and 293.8 eV corroborated to 1 s-π* and 1 s-σ* electronic transition of sp^2 hybridized carbons, trigonally bonded with nitrogen in tris-*s*-triazine moieties [81]. The presence of a strong π* signal in the C *K*-edge loss region demonstrates extended π conjugated orbitals in the tris-*s*-triazine ring system. Similarly, two peak components at 393.6 and 401.6 eV in N *K*-edge energy loss region were assigned to 1 s-π* and 1 s-σ* electronic transitions of sp^2 hybridized nitrogens of tris-*s*-triazine units/tertiary bridging nitrogens. Again the presence of intense π* signal in N *K*-edge loss region indicates a well-constituted carbon nitride framework [82]. Interestingly, after transformation of CN to CNM sheets, the N1s-π* and 1 s-σ* edge intensity was reduced due to the protonation of NH$_2$/NH groups resulting in decreased contribution of NH$_2$/NH lone pairs in aromatic heptazine network.[83] To probe the distribution of CNM all over the surface of CNMBr, STEM EDX elemental mapping line spectra were collected (Fig. 2o). The EDX line spectra clearly show the overlapped distributions of C and N on the Cs, Pb and Br signals of CsPbBr$_3$ nanocrystals validating the uniform distribution of CNM on CNMBr.

X-ray photoelectron spectroscopy (XPS) was employed to determine the surface/subsurface (~5 nm) chemical composition and binding energies of the constituent elements (Fig. 3). The XPS survey scans of CN, CNM and CNMBr displayed all the signature core level (CN: C1s, N1s and O1s; CNM: C1s, N1s and O1s and CNMBr: C1s, N1s, O1s, Cs3d, Pb4f, Br3d) and inner/sub-core-level (OKLL, O2s, Cs3p, Pb4p, Pb4d, Br3p) peaks of constituent elements verifying their presence in the composite materials (Fig. S7 in Supporting Information). The deconvoluted HR-XPS spectra of bulk CN displayed three peaks located at 284.8, 286.2 and 288.1 eV. The HR-XPS peak at 284.8 eV was assigned to sp^3 hybridized turbostratic adventitious carbons (C-C), while the peaks at BE≈ 286.2 and 288.1 eV originated respectively from sp^2 hybridized tertiary

(C-(N)$_3$) and secondary (N-C = N) aromatic carbons of heptazine units (C$_6$N$_7$) constituting the carbon nitride framework (Fig. 3a) [84,85]. After the transformation of bulk materials into sheets, the C1s XPS peaks remain identical for CNM suggesting intact CN framework in monolayer sheets. However, the peak corresponding to secondary carbons was broadened which might be due to signal contribution from the oxidized state carbons. CNMBr also displayed all the C1s peaks corresponding to various carbons of carbon nitride verifying the presence of CNM on the nanocrystal structure. The relative signal intensity of the C-C peak was increased due to the presence of sp^3 hybridized carbon from the aliphatic alkyl chain of ligands. The N1s core level HR-XPS spectra of CN after deconvolution displayed four peak components centered at 398.7, 399.6, 401.1 and 404.6 eV (Fig. 3c). The two intense peaks at 398.7 and 399.6 eV were corroborated to sp^2 hybridized secondary C = N–C and tertiary N–(C)$_3$ nitrogens of tris-*s*-triazine units of CN polymer while weak shoulder peak at 401.1 eV originated from sp^3 hybridized terminal/strand primary nitrogens (–NH$_2$/NH) (Fig. 3b) [77,86,87]. A very weak XPS signal at BE value 404.6 eV originated from π-π* transition in a conjugated CN system [88]. The three peaks due to secondary (C = N–C), tertiary (N–(C)$_3$) and primary nitrogens (–NH$_2$/NH) centered at 398.7, 399.6 and 401.1 eV remain identical for CNM samples. A slight shift of N–(C)$_3$ peak toward higher binding energy was attributed due to protonation of CN sheets resulting in decreased charge density on heptazine network. Additionally, an increment in CNM N–(C)$_3$ peak was attributed to reduction of other N's (N-C = N) intensity due to the partial oxidation which concomitantly increases the relative signal intensity of tertiary nitrogens. Interestingly, the π-π* transition peak for the CNM sample was intense and located at a relatively higher binding energy value (406.2 eV). Due to the quantum confinement effect in monolayer sheets, the HOMO-LUMO energy gap increased and larger energy is needed to promote π-π* transition resulting in the increased BE value while increased order/periodicity in CNM reduces the intersheet recombination and increases signal intensity. For CNMBr - in addition to the CNM peak, another peak was observed at 401.9 eV that might originate from primary nitrogens of alkyl amine (C-NH$_2$). Further, the XPS peak due to π-π* transition was completely absent for CNMBr suggesting faster charge transfer between CNM and CsPbBr$_3$ crystal.
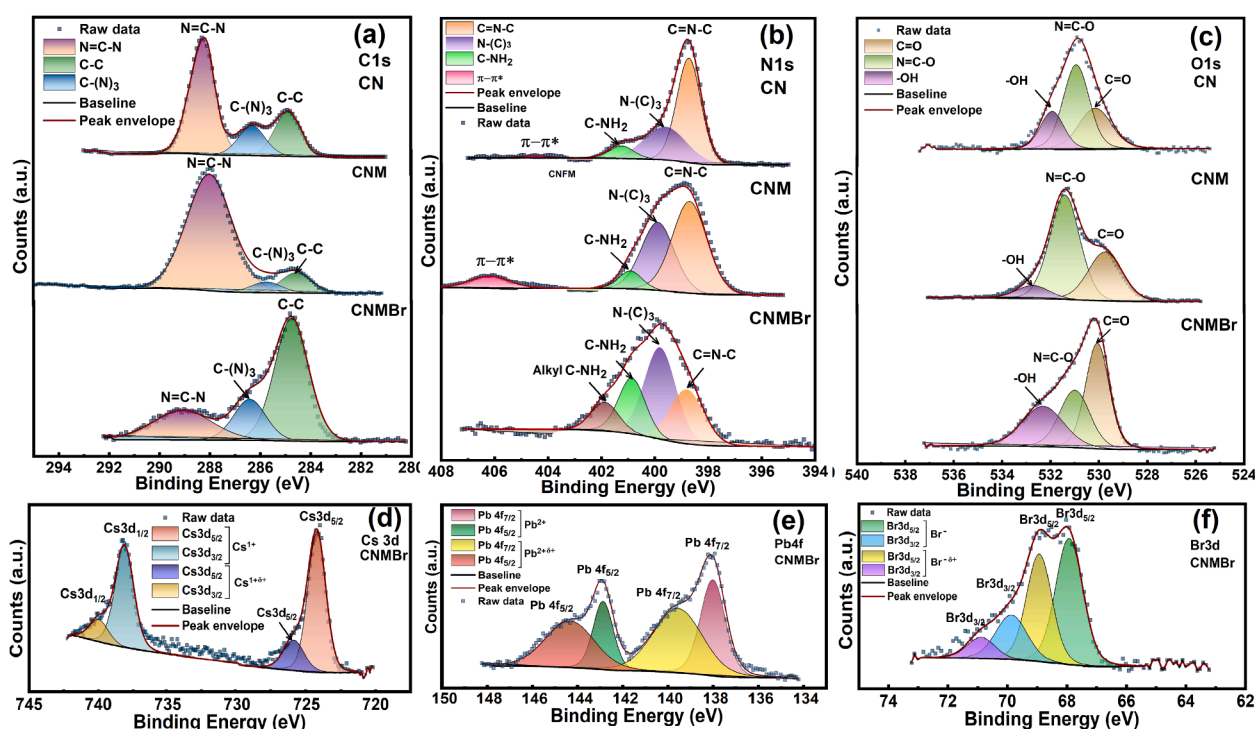

Fig. 3. Core-level HR-XPS spectra of CN, CNM, CNMBr in (a) C1s, (b) N1s, (c) O1s regions and HR-XPS spectra of CsPbBr$_3$ in (d) Cs3d, (e) Pb4f and (f) Br3d region.

The deconvoluted HR-XPS spectra of CN, CNM and CNMBr in the O1s region gave three peak components (CN: 530.1, 530.9, 531.9; CNM: 529.9, 531.5, 532.8; CNMBr: 530.0, 531.1, 532.3 eV) assigned to C = O, N = C-O of partially polymerized CN fragments and –OH of adventitious oxygen respectively (Fig. 3c) [89,90]. It is worthy to mention that the O1s peak for CNM and CNMBr was shifted to high BE value due to protonation of N = C-O (N = $C^{\delta+}$-$O^{\delta-}$—H^+). The deconvoluted XPS of CNMBr in the Cs3d region gave two well-resolved peaks at 724.2 and 738.1 eV due to $Cs3d_{5/2}$ and $Cs3d_{3/2}$ peak components of Cs present in + 1 oxidation state (Fig. 3d) [91]. Additionally, each peak comprised of a shoulder peak positioned at 725.9 and 740.0 eV. The shoulder peak at relatively high binding energy was originated due to partially charge transfer from Cs ions to positively charged CNM sheets. Two well-separated peaks at 138.0 and 142.9 eV for CNMBr in Pb4f regions arising from $Pb4f_{7/2}$ and $Pb4f_{5/2}$ peak components validates the presence of Pb in + 2 oxidation state (Fig. 3e) [92]. The appearance of broad shoulder peaks at 139.6 and 144.5 eV further verifies partial charge transfer to the CNM structure validating effective interaction. Two merged peak components in Br3d XPS of CNMBr at 67.9 and 69.0 eV corresponding to $Br3d_{5/2}$ and $Br3d_{3/2}$ components of for Br^- ion along with shoulder peaks demonstrate the presence of bromine as bromide in −1 and partially positive (δ +) oxidation state. (Fig. 3f) [93].

3.2. Optical absorption and fluorescence of halide perovskite colloidal nanoparticles, carbon nitride nanosheets, and CsPbBr3@CNM core-shell nanoparticles

The optical extinction spectra of solid/liquid dispersed in water/hexane and their thin films fabricated on the glass are shown in Fig. 4a. The UV–Vis spectra of CsPbBr3 nanocrystals suspended in hexane contained an excitonic absorption peak at 495 nm and an absorption band-edge at 520 nm (Fig. 4a) [33,57]. The diffuse reflectance UV–Vis (DR-UV–vis) spectra of CN displayed a strong absorption band in the 200–450 nm region with an absorption tail that extended to 600 nm. The absorption band in the 200–450 nm range originated from direct band-to-band transition between the valence band composed of N 2p orbitals and conduction band composed of C 2p orbitals. The relatively weak absorption peak at 290 nm in UV–Vis spectra of CN arises from $\pi \rightarrow \pi^*$ transition while another sharp absorption peak at 375 nm originated from n $\rightarrow \pi^*$ transition in the CN scaffold. The orbital overlap of amino functionalities creates low energy sublevels that facilitate longer wavelength transitions giving band tail absorption. After the transformation of bulk CN into monolayer CN sheets, the color changed from pale yellow to white (inset of Fig. 4a) and the optical absorption was significantly blue shifted with a band edge at ~ 415 nm. As

demonstrated in previous reports, the blue-shifted absorption in CNM sheets is due to the confinement effect and concomitant bandgap widening [60,94,95]. Previous theoretical calculations using DFT also demonstrated that when numbers of stacked sheets in carbon nitride approaches below four a drastic increment in bandgap is observed [96,97]. These observations confirm that the sheets synthesized using HNO3 assisted exfoliation were just one to three atomic layers thick.

The Bohr exciton radius a_B of CsPbBr3 is 3.5 nm due to which quantum confinement is not expected to occur in the CsPbBr3 nanocrystals synthesized in this work. The exciton binding energy in bulk CsPbBr3 crystals is reported to be 19–62 meV which is slightly larger than the values in other lead halide perovskites [98,99]. On the other hand, a rather large exciton binding energy of 350 meV has been measured in $23 \times 3 \times 4$ nm^3 nano-platelets of CsPbBr3. Pristine CsPbBr3 nanocrystals synthesized in this report with a size of ~ 20–25 nm (indicated by DLS and HRTEM) displayed a prominent excitonic feature centered at ~ 480 nm (Fig. S7 in Supporting Information), which is remarkably similar to the 480 nm lowest energy exciton band observed in the UV–Vis spectrum of ~ 7 nm sized cubical CsPbBr3 quantum dots [30]. It is conceivable that while one dimension of the CsPbBr3 quantum dots is ~ 20–25 nm in size, one or both of the remaining two dimensions are smaller in size than a_B. The CNMBr containing *in situ* CNM coupled CsPbBr3 displayed a sharp band edge at 550 nm with a small excitonic feature at 512 nm (red curve in Fig. 4a). Compared to pristine CsPbBr3, a remarkable 30 nm redshift in the absorption edge occurred which we attribute to the delocalization of charge carriers over the entire core and shell, which is reminiscent of the redshift in organic semiconductors induced by an increase in the conjugation length.

Photoluminescence (PL) spectroscopy was employed for the determination of the recombination dynamics of photogenerated charge carriers. The representative steady-state PL spectra of the liquid colloidal suspensions and thin films are given in Fig. 4b and its inset. The CsPbBr3 nanocrystals displayed bright green photoluminescence under 365 nm excitation both in colloidal suspensions in hexane and in thin films deposited on a glass slide. The strong fluorescence of CsPbBr3 thin films suggests the absence of aggregation and concentration quenching. Fluorescence microscope images of CsPbBr3 deposited on a glass slide under 480 nm excitation wavelength displayed bright fluorescence emission at 530 nm (Fig. S6 a, b in Supporting Information). The PL spectra of pristine CsPbBr3 nanocrystals exhibited an exclusive PL peak centered at 500 nm due to band-to-band recombination within the crystal lattice [57]. The broad intense PL peak of bulk carbon nitride located at 463 nm originated from colossal interband and intersheet recombination. Fluorescence microscope images of CN collected by exciting samples under 350 and 535 nm and measuring emission at 460
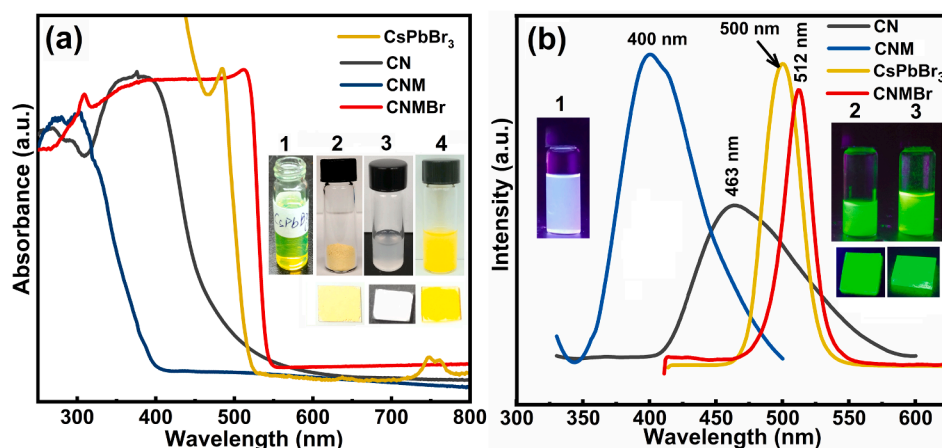

Fig. 4. (a) DR-UV–Vis spectra of CN, CNM, CNMBr, Insets 1, 2, 3and 4 showing digital photographs of the CsPbBr3, CN, CNM (in water), CNMBr and their films on glass. (b) Steady-state PL (ssPL) spectra of CsPbBr3 nanocrystals, CN, CNM, CNMBr, Inset 1, 2 and 3, showing fluorescence image of CNM, CsPbBr3 and CNMBr images their thin film on glass under 365 nm light **Color:** CsPbBr3, (yellow), CN (black), CNM (cyan), CNMBr (red).

and 610 nm respectively validated the broad PL response of CN (Fig. S6) [100,101]. The intensity of images collected by monitoring the 610 nm emission was relatively weak due to weak band edge excitation at 535 nm. The monolayered CNM sheets showed an intense PL peak centered at 400 nm [60]. The huge blueshift in the PL peak position demonstrates an increased bandgap which was in good agreement with the UV–Vis absorption spectrum. The PL peak of CNMBr at 512 nm was red-shifted compared to pristine $CsPbBr_3$ suggesting bandgap reduction in harmony with the red-shift in the optical absorption. CNMBr shows a very low Stokes shift of < 1 nm, which indicates low disorder, and is supportive of carrier delocalization over the core–shell structure. Two-photon fluorescence imaging (FLIM) lifetime measurements were performed on CN and CNM samples to calculate the PL lifetime of excited species (see Section 3 in Supporting information for details). The average lifetimes (τ_{ave}) calculated by the tri-exponential fitting of FLIM lifetime curve were found to be 1.14 and 1.72 ns for CN and CNM samples respectively (Fig. S12 and Table S1 in Supporting Information). The increased average lifetime value of CNM was because of the increase in intrasheet order and significant inhibition of intersheet recombination following the transformation of bulk CN into monolayer sheets [102,103].

3.3. Photoelectrochemical water splitting using core-shell CNMBr nanocrystals

Photoelectrochemical (PEC) water splitting, and CO_2 reduction experiments were performed to examine the ability of CNMBr core-shell nanoparticles to photocatalytically produce solar fuels. For PEC measurements, a standard three-electrode setup consisting of an illuminated working electrode (photoanode), Pt cathode (counter electrode) and Ag/AgCl reference electrode was used. The working electrode consisted of CN, CNM and CNMBr materials deposited on FTO. The measurements were carried out under AM1.5 G simulated sunlight (100 mW cm^{-1}) with and without UV cut-off long-pass filter (λ > 420 nm) using 0.1 M Na_2SO_4 as the electrolyte. The photoresponse and photocurrent density of materials during light On-Off cycles as a function of time (*i-t* curve) were measured at an applied bias of + 0.6 V *vs* Ag/AgCl. Among all the samples, CNMBr displayed the highest photocurrent density reaching up to 1.55 mA cm^{-2} (Fig. 5b and Fig. S14 in Supporting Information). CNM samples produced double the photocurrent density of CN samples even though the transformation of bulk sheets into monolayered sheets severely reduced visible light absorption suggesting better charge separation on crystalline carbon nitride nanosheets (CNM). The small semicircle for CNM compared to CN in the EIS Nyquist plot (Fig. S13d in Supporting Information) verifies that the charge transfer resistance was decreased after transformation of bulk materials into sheets promoting faster transfer of photogenerated holes to hydroxide and oxide anions in the electrolyte [104]. The photoelectrochemical outperformance of CNMBr samples is attributed to excellent visible absorption and longer

carrier migration length in $CsPbBr_3$ nanocrystals. Additionally, the shell of CNM sheets facilitates the extraction of photogenerated holes from the core $CsPbPb_3$ nanocrystals through their extended conjugated network, which then proceed to oxidize electrolyte species. Scanning Kelvin Probe Force Microscopy (KPFM) confirmed that for blue light excitation, the surface of the sample became acquired a more positive potential w.r.t the dark, which is indicative of hole extraction by the CNM shell from the $CsPbBr_3$ core (Fig. 6). Electrons on the other hand likely tunnel from one $CsPbBr_3$ nanocrystal to another through the 1–3 atom layer CNM shell layer under the applied anodic bias and reach the FTO electron collector (and subsequently pass through the external circuit to reduce protons in the electrolyte at the cathode). Linear sweep voltammograms (LSV) to measure the photoresponse of materials with respect to dark conditions were collected by sweeping the applied voltage in the range of −1.0 to + 1.0 V *vs* Ag/AgCl (Fig. S17-S19 in Supporting Information). All three samples provided instantaneous photoresponse during the light On-Off cycles. To probe the response of the materials under longer wavelength irradiation, the photocurrent density of materials *vs* time was measured using monochromatic 365, 420, 460, 520, 580 and 640 nm wavelength LEDs (Fig. S17-S19 in Supporting Information). All the materials demonstrated a longer wavelength response up to 580 nm with the maximum photocurrent density for the CNMBr sample at 365 nm followed by 420 nm. The maximum blue light response of the CNMBr samples was also evident from surface potential measurement determined using KPFM (Fig. 6).

3.4. Vapor phase CO_2 photoreduction using core-shell CNMBr nanocrystals

For CO_2 photoreduction experiments, CN, CNM and CNMBr samples spin-coated on a 1 × 1 cm^2 glass slides were placed in a cylindrical stainless steel reactor (30 mL internal volume, quartz top window) followed by the addition of 200 μL of DI water. The reactor was purged many times with N_2 followed by CO_2. Following purging, a CO_2 pressure of 50 psi was maintained. The reactor was heated at 80 °C to saturate the chamber with water vapor and finally irradiated under AM1.5 G solar simulated light for 2 h. It is important to note that a sacrificial agent such as triethanolamine was not employed for CO_2 photoreduction. The gaseous reaction product was analyzed using gas chromatography (Shimadzu gas chromatograph; GC-2014) equipped with a Porapak Q/Mol Sieve column, and a pulsed discharge detector (PDD). CN and CNM as photocatalysts did not generate any CO_2 reduction products, though a negligible amount of hydrogen was observed as expected. However, gas product analysis of the CNMBr sample demonstrated CO, CH_4 and H_2 as major CO_2 reduction products. The yield of CO, CH_4 and H_2 expressed in μmol cm$^{-2}_{cat}$ were found to be 0.407, 0.104 and 0.008 μmol cm$^{-2}_{cat}$ respectively (Fig. 7). To ensure that CO_2 reduction was truly photocatalytic and not because of thermal reaction or photodegradation of
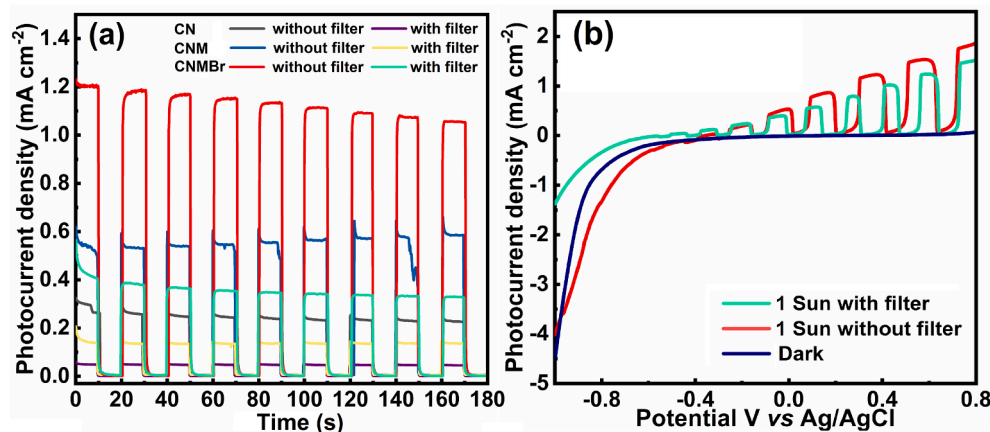

Fig. 5. (a) Photocurrent density *vs* time (*J-t*) plot for CN, CNM and CNMBr showing photoresponse during light On-Off cycle at + 0.6 V applied bias, under solar simulated AM1.5G light irradiation without filter (100 mW cm^{-2}) with and AM1.5G light irradiation with a 420 nm cut-off filter (b) *J-V* curve during light On-Off cycle for CN, CNM and CNMBr under AM1.5G light irradiation without filter (100 mW cm^{-2}) and AM1.5G light irradiation with a 420 nm cut-off long pass filter. **Color:** 1 Sun without filter: CN (gray), CNM (blue), CNMBr (red) and 1 Sun with filter: CN (violet), CNM (yellow), CNMBr (cyan). All the measurements were performed in 0.1 M Na_2SO_4 solution at a scan rate of 0.1 mV/sec.
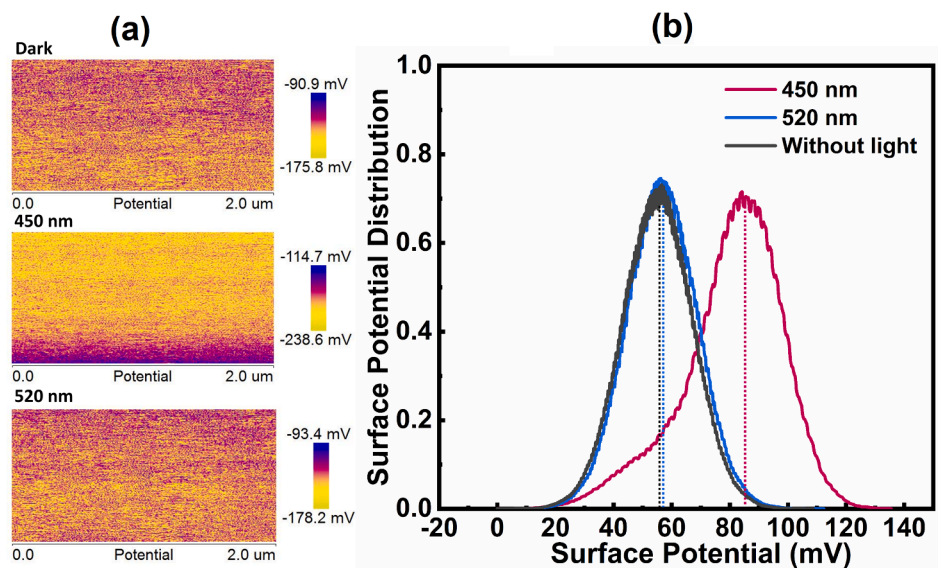
Fig. 6. (a) Surface potential maps of FTO deposited CNMBr samples under dark, 450 and 635 nm laser, (b) The surface potential distribution of FTO deposited CNMBr samples under dark (black), 450 nm (pink) and 520 nm (blue).
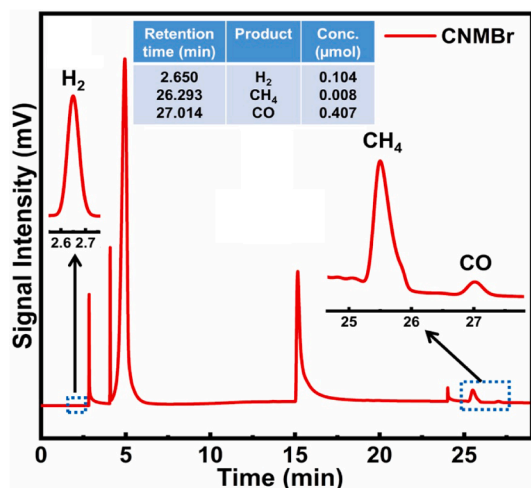

Fig. 7. GC chromatogram of CO_2 reduction products and their relative distribution.

organic contaminants in the sample, blank experiments were carried out 1) In the absence of photocatalyst, 2) Under dark reaction and 3) Using N_2 instead of CO_2. No trace of any CO_2 reduction product was identified in the control experiments which confirms that the reaction products originated from the photoreduction of CO_2. Further, isotopic labeling experiments using $^{13}CO_2$ instead of $^{12}CO_2$ gave ^{13}C labeled products to confirm the origin of CO and CH_4 from photoreduction of CO_2 (Fig. S18 and S19 in Supporting Information).

The increased photocatalytic performance of the CNMBr can be explained based on perovskite structural stabilization, increased crystallinity of carbon nitride, lower charge transfer resistance, more negative conduction band and synergistic interactions. Although previous reports mentioned the stabilization of perovskite nanocrystals using carbon nitride and graphene materials [38,49,105–107], their photocatalytic performance was sub-optimal because bulk carbon nitride always comes with the drawback of extensive intersheet charge recombination. In this work, we used nearly monolayer carbon nitride for the protection of $CsPbBr_3$ nanocrystals which prevented charge recombination on its surface. Since an *in situ* approach was used for the

synthesis of CNMBr nanocomposite, better surface passivation was achieved resulting in improved charge carrier mobility. Such an effect has been previously reported for the carbon nitride/perovskite systems in solar cell devices where PCE was increased due to better crystallization and minimization of grain boundaries, and the conjugated surface provided pathways for electron movements [50,51,108]. In addition to better charge transport on CN sheets, since the CNM shell was < 5 nm thick as confirmed by HR-TEM images, the photogenerated electrons in the $CsPbBr_3$ core can reach the FTO electron collection electrode *via* tunneling under applied anodic bais (in photoelectrochemical water splitting) or react with protons that permeate through the CNM shell (in CO_2 photoreduction). Previous reports demonstrated that carbon nitride is permeable to protons while at the same time it blocks oxygen, CO_2, N_2 and moisture from penetrating into the perovskite core keeping perovskite stable [55,56,109–111]. The protons can percolate to the perovskite surface *via* interstitial cavity of carbon nitride which after receiving electrons produces hydrogen. Another potential mechanism for the utilization of photogenerated electrons involves the delocalization of electrons over the entire core-shell structure, which is supported by the low Stokes shift and large (~30 nm) redshift in the absorption edge of CNMBr core-shell nanocrystals. Such delocalization of charge carriers would enable both electrons and holes to be readily available at the CNM surface for photocatalytic and photoelectrochemical reactions.

The electron-rich surface of carbon nitride due to the presence of secondary and tertiary nitrogens possessing lone pair of electrons behaves as a Lewis base, and electron-deficient CO_2 which has weak Lewis acid character can bind to the surface of CNMBr more strongly increasing the availability of CO_2 for photoreaction [112,113]. Indeed, the biggest challenge is poor CO_2 adsorption on the surface of catalysts (particularly halide perovskites) and water always competes for the generated electrons producing hydrogen as a by-product. Further, in comparison to bulk carbon nitride, the formed CNM has a more ordered and periodic structure reducing localized charge recombination [71,72,74,114]. This fact was confirmed by the PL lifetime decay curve which shows increased average lifetime due to better stabilization and mobility of photogenerated charge on the surface of carbon nitride sheets [103,115]. Further, the EIS Nyquist plot also shows a much smaller semicircle arc for CNM compared to CN suggesting decreased charge transfer resistance which improves charge transfer probability in between the active material and electrolyte. As for the efficient reduction of the protons to hydrogen (H^+/H_2), the CB band position of the

semiconductor should be more negative than 0.00 V *vs* NHE at pH-7 (water reduction potential) while for reduction of CO_2 to CH_4 and CO the conduction band should be more negative than -0.24 V (CO_2/CH_4) and -0.53 V (CO_2/CO) *vs* NHE, respectively. For self-sustained water splitting, the protons and electrons should derive from water oxidation, so the valence band should be more positive than $+1.23$ V *vs* NHE (water oxidation potential; H_2O/O_2). Considering Fermi level was close to conduction band the CB position of CNMBr was found to be -0.75 V *vs* Ag/AgCl or -0.57 V *vs* NHE. This demonstrates that CNMBr can efficiently reduce water and CO_2 to produce CO, H_2 and CH_4.

4. Conclusion

The *in situ* growth of $CsPbBr_3$ nanocrystal in the presence of mono-layered carbon nitride has afforded air and water stable and passivated perovskite nanocrystals. The core-shell CNMBr nanocrystals are stable in air, water and polar solvents for over two months and retain their fluorescence for this duration. The particle size distribution of $CsPbBr_3$ nanocrystal in the CNM matrix was mostly uniform, however, some smaller spherical particles were also observed. The CN sheets formed by HNO_3 promoted exfoliation and disrupted intersheets hydrogen bonding show increased crystallinity after solvent removal due to more ordered stacking. The FTIR and Raman spectra of carbon nitride were simulated using a quantum chemistry package and then compared with the experimental vibrational spectra to confirm the presence of the carbon nitride framework in the CNM nanosheets following exfoliation and shell formation. Strong spectroscopic evidence was found indicating increased crystallinity and lower disorder in the CNM shell. The CNMBr nanocomposite due to decreased defect density and better passivation provides a path for efficient charge migration. When used as a photo-anode in photoelectrochemical water splitting, the CNMBr demon-strated a photocurrent value of 1.55 mA cm^{-2}. KPFM data confirmed preferential extraction of photogenerated holes in the $CsPbBr_3$ core by the CNM shell. The CNMBr can also activate CO_2 to transform into small molecules such as CO and CH_4 without the need for scavengers such as triethanolamine or ethanol. Built-in potential differences at the core-shell interface that promote extraction of holes through a lower unoc-cupied energy level in the shell materials or drive tunneling of electrons outward through the shell also cause electrons to remain in the core. Therefore, efficient extraction of both electrons and holes from the halide perovskite core of such core-shell systems is prohibitively diffi-cult. However, CNMBr core-shell nanocrystals are able to substantially overcome this challenge as indicated by the photoelectrochemical and photocatalytic data in this work.

CRediT authorship contribution statement

Devika Laishram: Conceptualization, Methodology, Formal anal-ysis, Investigation, Writing – original draft. **Sheng Zeng:** Investigation, Methodology, Formal analysis. **Kazi M. Alam:** Investigation, Method-ology. **Aarat P. Kalra:** Investigation, Methodology, Validation. **Kai Cui:** Investigation, Formal analysis. **Pawan Kumar:** Methodology, Formal analysis, Investigation, Visualization, Writing – original draft. **Rakesh K. Sharma:** Writing – review & editing, Supervision, Funding acquisi-tion. **Karthik Shankar:** Conceptualization, Writing – review & editing, Visualization, Supervision, Project administration, Funding acquisition, Resources.

Declaration of Competing Interest

The authors declare that they have no known competing financial interests or personal relationships that could have appeared to influence the work reported in this paper.

Appendix A. Supplementary material

Additional experimental details; review of approaches toward achieving single layer carbon nitride; electron micrographs (Fig. S1-S5); fluorescence microscope images (Fig. S6); XPS survey scan, XRD pat-terns, DLS plot, experimental and simulated Raman and FTIR spectra, FLIM lifetime decay curve, Mott-Schottky and Nyquist plot (Fig. S7-S13); KPFM measurement protocol; PEC water splitting results - LSV, *i-t* curve under AM 1.5G irradiation and LEDs (Fig. S14-S17); Isotope-labeled mass spectrometric data (Fig. S18-S19); Interfacial band-alignment including XPS valence band spectra and UPS spectra (Fig. S20); Proposed band-diagram at $CsPbBr_3$-CNM interface (Fig. S21). Supplementary data to this article can be found online at https://doi.org /10.1016/j.apsusc.2022.153276.

References

[1] Y. Liang, S. Tsuji, J. Jia, T. Tsuji, T. Matsuoka, Modeling CO_2–water–mineral wettability and mineralization for carbon geosequestration, Acc. Chem. Res. 50 (2017) 1530–1540.

[2] M.S. Kareya, I. Mariam, A. Arumugam Nesamma, P.P. Jutur, CO_2 sequestration by hybrid integrative photosynthesis (CO_2-SHIP): A green initiative for multi-product biorefineries, Mater. Sci. Energy Technol. 3 (2020) 420–428.

[3] G.A. Olah, Towards oil independence through renewable methanol chemistry, Angew. Chem. Int. Ed. 52 (2013) 104–107.

[4] M. Aresta, A. Dibenedetto, Utilisation of CO_2 as a chemical feedstock: opportunities and challenges, Dalton Trans. (28) (2007) 2975–2992.

[5] K. Başaran, B.U. Topçubaşı, T. Davran-Candan, Theoretical investigation of CO_2 adsorption mechanism over amine-functionalized mesoporous silica, J. CO2 Util. 47 (2021) 101492.

[6] A. Listorti, J. Durrant, J. Barber, Artificial photosynthesis: solar to fuel, Nat. Mater. 8 (12) (2009) 929–930.

[7] N.S. Lewis, Developing a scalable artificial photosynthesis technology through nanomaterials by design, Nat. Nanotechnol. 11 (2016) 1010.

[8] S. Albrecht, B. Rech, Perovskite solar cells: On top of commercial photovoltaics, Nat. Energy 2 (2017) 16196.

[9] J. Wei, Q. Ge, R. Yao, Z. Wen, C. Fang, L. Guo, H. Xu, J. Sun, Directly converting CO_2 into a gasoline fuel, Nat. Commun. 8 (2017) 15174.

[10] W. Ning, N. Koizumi, M. Yamada, Researching Fe catalyst suitable for CO_2-containing syngas for Fischer– Tropsch synthesis, Energy Fuels 23 (2009) 4696–4700.

[11] Y. Tachibana, L. Vayssieres, J.R. Durrant, Artificial photosynthesis for solar water-splitting, Nat. Photonics 6 (8) (2012) 511–518.

[12] A. Kumar, P. Kumar, S.L. Jain, Nanostructured Composite Materials for CO_2 Activation, Advances in Nanostructured Composites: Volume 1: Carbon Nanotube and Graphene Composites, (2019) 174.

[13] J.L. White, M.F. Baruch, J.E. Pander, Y. Hu, I.C. Fortmeyer, J.E. Park, T. Zhang, K. Liao, J. Gu, Y. Yan, T.W. Shaw, E. Abelev, A.B. Bocarsly, Light-driven heterogeneous reduction of carbon dioxide: photocatalysts and photoelectrodes, Chem. Rev. 115 (23) (2015) 12888–12935.

[14] J.J. Concepcion, R.L. House, J.M. Papanikolas, T.J. Meyer, Chemical approaches to artificial photosynthesis, Proc. Natl. Acad. Sci. 109 (39) (2012) 15560–15564.

[15] X. Li, Y. Sun, J. Xu, J. Shao, J.u. Wu, X. Xu, Y. Pan, H. Ju, J. Zhu, Y.i. Xie, Selective visible-light-driven photocatalytic CO_2 reduction to CH_4 mediated by atomically thin $CuIn_5S_8$ layers, Nat. Energy 4 (8) (2019) 690–699.

[16] S. Chen, T. Takata, K. Domen, Particulate photocatalysts for overall water splitting, Nat. Rev. Mater. 2 (2017) 17050.

[17] S.S. Mao, S. Shen, Hydrogen production: catalysing artificial photosynthesis, Nat. Photonics 7 (2013) 944.

[18] H. Inoue, T. Shimada, Y. Kou, Y. Nabetani, D. Masui, S. Takagi, H. Tachibana, The water oxidation bottleneck in artificial photosynthesis: How can we get through

it? an alternative route involving a two-electron process, ChemSusChem 4 (2011) 173–179.

[19] X. Liu, S. Inagaki, J. Gong, Heterogeneous molecular systems for photocatalytic CO$_2$ reduction with water oxidation, Angew. Chem. Int. Ed. 55 (2016) 14924–14950.

[20] P. Kar, S. Zeng, Y. Zhang, E. Vahidzadeh, A. Manuel, R. Kisslinger, K.M. Alam, U. K. Thakur, N. Mahdi, P. Kumar, High rate CO$_2$ photoreduction using flame annealed TiO$_2$ nanotubes, Appl. Catal. B 243 (2019) 522–536.

[21] P. Kumar, C. Joshi, A. Barras, B. Sieber, A. Addad, L. Boussekey, S. Szunerits, R. Boukherroub, S.L. Jain, Core–shell structured reduced graphene oxide wrapped magnetically separable rGO@ CuZnO@Fe$_3$O$_4$ microspheres as superior photocatalyst for CO$_2$ reduction under visible light, Appl. Catal. B 205 (2017) 654–665.

[22] S.N. Habisreutinger, L. Schmidt-Mende, J.K. Stolarczyk, Photocatalytic reduction of CO$_2$ on TiO$_2$ and other semiconductors, Angew. Chem. Int. Ed. 52 (2013) 7372–7408.

[23] Z. Wang, C. Li, K. Domen, Recent developments in heterogeneous photocatalysts for solar-driven overall water splitting, Chem. Soc. Rev. 48 (2019) 2109–2125.

[24] M. Anaya, A. Rubino, T.C. Rojas, J.F. Galisteo-López, M.E. Calvo, H. Míguez, Strong quantum confinement and fast photoemission activation in CH$_3$NH$_3$PbI$_3$ perovskite nanocrystals grown within periodically mesostructured films, Adv. Opt. Mater. 5 (2017) 1601087.

[25] F. Zhang, S. Huang, P. Wang, X. Chen, S. Zhao, Y. Dong, H. Zhong, Colloidal synthesis of air-stable CH$_3$NH$_3$PbI$_3$ quantum dots by gaining chemical insight into the solvent effects, Chem. Mater. 29 (2017) 3793–3799.

[26] F. Zhang, H. Zhong, C. Chen, X.-G. Wu, X. Hu, H. Huang, J. Han, B. Zou, Y. Dong, Brightly luminescent and color-tunable colloidal CH$_3$NH$_3$PbX$_3$ (X= Br, I, Cl) quantum dots: potential alternatives for display technology, ACS Nano 9 (4) (2015) 4533–4542.

[27] Z. Zheng, F. Zhuge, Y. Wang, J. Zhang, L. Gan, X. Zhou, H. Li, T. Zhai, Decorating perovskite quantum dots in TiO$_2$ nanotubes array for broadband response photodetector, Adv. Funct. Mater. 27 (43) (2017) 1703115.

[28] S. Sun, D. Yuan, Y. Xu, A. Wang, Z. Deng, Ligand-mediated synthesis of shape-controlled cesium lead halide nanocrystals via reprecipitation process at room temperature, ACS Nano 10 (3) (2016) 3648–3657.

[29] G.e. Gao, Q. Xi, H. Zhou, Y. Zhao, C. Wu, L. Wang, P. Guo, J. Xu, Novel inorganic perovskite quantum dots for photocatalysis, Nanoscale 9 (33) (2017) 12032–12038.

[30] K. Wu, G. Liang, Q. Shang, Y. Ren, D. Kong, T. Lian, Ultrafast interfacial electron and hole transfer from CsPbBr 3 perovskite quantum dots, J. Am. Chem. Soc. 137 (40) (2015) 12792–12795.

[31] X. Li, Y.e. Wu, S. Zhang, B.o. Cai, Y.u. Gu, J. Song, H. Zeng, CsPbX$_3$ quantum dots for lighting and displays: room-temperature synthesis, photoluminescence superiorities, underlying origins and white light-emitting diodes, Ad. Funct. Mater. 26 (15) (2016) 2435–2445.

[32] Z.-C. Kong, J.-F. Liao, Y.-J. Dong, Y.-F. Xu, H.-Y. Chen, D.-B. Kuang, C.-Y. Su, Core@Shell CsPbBr 3@Zeolitic imidazolate framework nanocomposite for efficient photocatalytic CO$_2$ reduction, ACS Energy Lett. 3 (11) (2018) 2656–2662.

[33] J.-F. Liao, J.-F. Xu, X.-D. Wang, H.-Y. Chen, D.-B. Kuang, CsPbBr 3 nanocrystal/MO$_2$ (M= Si, Ti, Sn) composites: insight into charge-carrier dynamics and photoelectrochemical applications, ACS Appl. Mater. Interfaces 10 (49) (2018) 42301–42309.

[34] Y.-F. Xu, X.-D. Wang, J.-F. Liao, B.-X. Chen, H.-Y. Chen, D.-B. Kuang, Amorphous-TiO$_2$-encapsulated CsPbBr 3 nanocrystal composite photocatalyst with enhanced charge separation and CO$_2$ fixation, Adv. Mater. Interfaces 5 (22) (2018) 1801015.

[35] Z. Li, L. Kong, S. Huang, L. Li, Highly luminescent and ultrastable CsPbBr 3 perovskite quantum dots incorporated into a silica/alumina monolith, Angew. Chem. Int. Ed. 56 (28) (2017) 8134–8138.

[36] T. Xuan, X. Yang, S. Lou, J. Huang, Y. Liu, J. Yu, H. Li, K.-L. Wong, C. Wang, J. Wang, Highly stable CsPbBr 3 quantum dots coated with alkyl phosphate for white light-emitting diodes, Nanoscale 9 (40) (2017) 15286–15290.

[37] J. De Roo, M. Ibáñez, P. Geiregat, G. Nedelcu, W. Walravens, J. Maes, J. C. Martins, I. Van Driessche, M.V. Kovalenko, Z. Hens, Highly dynamic ligand binding and light absorption coefficient of cesium lead bromide perovskite nanocrystals, ACS Nano 10 (2) (2016) 2071–2081.

[38] Y.-F. Xu, M.-Z. Yang, B.-X. Chen, X.-D. Wang, H.-Y. Chen, D.-B. Kuang, C.-Y. Su, A CsPbBr 3 perovskite quantum dot/graphene oxide composite for photocatalytic CO$_2$ reduction, J. Am. Chem. Soc. 139 (16) (2017) 5660–5663.

[39] Y. Wu, P. Wang, X. Zhu, Q. Zhang, Z. Wang, Y. Liu, G. Zou, Y. Dai, M.-H. Whangbo, B. Huang, Composite of CH$_3$NH$_3$PbI$_3$ with reduced graphene oxide as a highly efficient and stable visible-light photocatalyst for hydrogen evolution in aqueous HI solution, Adv. Mater. 30 (7) (2018) 1704342.

[40] P. Kumar, R. Boukherroub, K. Shankar, Sunlight-driven water-splitting using two-dimensional carbon based semiconductors, J. Mater. Chem. A 6 (27) (2018) 12876–12931.

[41] M. Faraji, M. Yousefi, S. Yousefzadeh, M. Zirak, N. Naseri, T.H. Jeon, W. Choi, A. Z. Moshfegh, Two-dimensional materials in semiconductor photoelectrocatalytic systems for water splitting, Energy Environ. Sci. 12 (2019) 59–95.

[42] I. Roger, M.A. Shipman, M.D. Symes, Earth-abundant catalysts for electrochemical and photoelectrochemical water splitting, Nat. Rev. Chem. 1 (2017) 0003.

[43] S.N. Talapaneni, G. Singh, I.Y. Kim, K. AlBahily, A.H. Al-Muhtaseb, A.S. Karakoti, E. Tavakkoli, A. Vinu, Nanostructured carbon Nitrides for CO$_2$ capture and conversion, Adv. Mater. 32 (18) (2020) 1904635.

[44] W.-J. Ong, L.-L. Tan, Y.H. Ng, S.-T. Yong, S.-P. Chai, Graphitic carbon nitride (g-C$_3$N$_4$)-based photocatalysts for artificial photosynthesis and environmental remediation: are we a step closer to achieving sustainability? Chem. Rev. 116 (2016) 7159–7329.

[45] Z. Jiang, H. Sun, T. Wang, B. Wang, W. Wei, H. Li, S. Yuan, T. An, H. Zhao, J. Yu, Nature-based catalyst for visible-light-driven photocatalytic CO$_2$ reduction, Energy Environ. Sci. 11 (2018) 2382–2389.

[46] K.M. Alam, P. Kumar, P. Kar, U.K. Thakur, S. Zeng, E. Vahidzadeh, K. Cui, K. Shankar, Heterojunctions of halogen-doped carbon nitride nanosheets and BiOI for sunlight-driven water-splitting, Nanotechnology 31 (2019) 084001.

[47] P. Kumar, P. Kar, A.P. Manuel, S. Zeng, U.K. Thakur, K.M. Alam, Y. Zhang, R. Kisslinger, K. Cui, G.M. Bernard, V.K. Michaelis, K. Shankar, Noble metal free, visible light driven photocatalysis using TiO$_2$ nanotube arrays sensitized by P-doped C$_3$N$_4$ quantum dots, Adv. Opt. Mater. 8 (2020) 1901275.

[48] J. Zhang, Y. Chen, X. Wang, Two-dimensional covalent carbon nitride nanosheets: synthesis, functionalization, and applications, Energy Environ. Sci. 8 (11) (2015) 3092–3108.

[49] S. You, S. Guo, X. Zhao, M. Sun, C. Sun, Z. Su, X. Wang, All-inorganic perovskite/graphitic carbon nitride composites for CO$_2$ photoreduction into C1 compounds under low concentrations of CO$_2$, Dalton Trans. 48 (2019) 14115–14121.

[50] P. Kumar, E. Vahidzadeh, U.K. Thakur, P. Kar, K.M. Alam, A. Goswami, N. Mahdi, K. Cui, G.M. Bernard, V.K. Michaelis, C$_3$N$_5$: A low bandgap semiconductor containing an azo-linked carbon nitride framework for photocatalytic, photovoltaic and sdsorbent applications, J. Am. Chem. Soc. 141 (2019) 5415–5436.

[51] X. Chen, Q. Liu, Q. Wu, P. Du, J. Zhu, S. Dai, S. Yang, Incorporating graphitic carbon nitride (g-C$_3$N$_4$) quantum dots into bulk-heterojunction polymer solar cells leads to efficiency enhancement, Adv. Funct. Mater. 26 (11) (2016) 1719–1728.

[52] Q.-F. Deng, L. Liu, X.-Z. Lin, G. Du, Y. Liu, Z.-Y. Yuan, Synthesis and CO$_2$ capture properties of mesoporous carbon nitride materials, Chem. Eng. J. 203 (2012) 63–70.

[53] Y. Oh, V.-D. Le, U.N. Maiti, J.O. Hwang, W.J. Park, J. Lim, K.E. Lee, Y.-S. Bae, Y.-H. Kim, S.O. Kim, Selective and regenerative carbon dioxide capture by highly polarizing porous carbon nitride, ACS Nano 9 (9) (2015) 9148–9157.

[54] S.W. de Silva, A. Du, W. Senadeera, Y. Gu, Strained graphitic carbon nitride for hydrogen purification, J. Membr. Sci. 528 (2017) 201–205.

[55] L. Yang, X. Li, G. Zhang, P. Cui, X. Wang, X. Jiang, J. Zhao, Y. Luo, J. Jiang, Combining photocatalytic hydrogen generation and capsule storage in graphene based sandwich structures, Nat. Commun. 8 (2017) 16049.

[56] Y. Ji, H. Dong, H. Lin, L. Zhang, T. Hou, Y. Li, Heptazine-based graphitic carbon nitride as an effective hydrogen purification membrane, RSC Adv. 6 (57) (2016) 52377–52383.

[57] L. Protesescu, S. Yakunin, M.I. Bodnarchuk, F. Krieg, R. Caputo, C.H. Hendon, R. X. Yang, A. Walsh, M.V. Kovalenko, Nanocrystals of cesium lead halide perovskites (CsPbX$_3$, X= Cl, Br, and I): novel optoelectronic materials showing bright emission with wide color gamut, Nano Lett. 15 (6) (2015) 3692–3696.

[58] S.C. Yan, Z.S. Li, Z.G. Zou, Photodegradation performance of g-C$_3$N$_4$ fabricated by directly heating melamine, Langmuir 25 (17) (2009) 10397–10401.

[59] K.M. Alam, P. Kumar, P. Kar, U.K. Thakur, S. Zeng, K. Cui, K. Shankar, Enhanced charge separation in g-C$_3$N$_4$–BiOI heterostructures for visible light driven photoelectrochemical water splitting, Nanoscale Adv. 1 (2) (2019) 1460–1471.

[60] J. Zhang, M. Zhang, L. Lin, X. Wang, Sol processing of conjugated carbon nitride powders for thin-film fabrication, Angew. Chem. Int. Ed. 54 (21) (2015) 6297–6301.

[61] U.K. Thakur, A.M. Askar, R. Kisslinger, B.D. Wiltshire, P. Kar, K. Shankar, Halide perovskite solar cells using monocrystalline TiO$_2$ nanorod arrays as electron transport layers: impact of nanorod morphology, Nanotechnology 28 (2017) 274001.

[62] P. Kumar, E. Vahidzadeh, U.K. Thakur, P. Kar, K.M. Alam, A. Goswami, N. Mahdi, K. Cui, G.M. Bernard, V.K. Michaelis, K. Shankar, C$_3$N$_5$: A low bandgap semiconductor containing an azo-linked carbon nitride framework for photocatalytic, photovoltaic and adsorbent applications, J. Am. Chem. Soc. 141 (2019) 5415–5436.

[63] X. Zhang, F. Han, B. Shi, S. Farsinezhad, G.P. Dechaine, K. Shankar, Photocatalytic conversion of diluted CO$_2$ into light hydrocarbons using periodically modulated multiwalled nanotube arrays, Angew. Chem. Int. Ed. 51 (2012) 12732–12735.

[64] S. Zeng, E. Vahidzadeh, C.G. VanEssen, P. Kar, R. Kisslinger, A. Goswami, Y. Zhang, N. Mahdi, S. Riddell, A.E. Kobryn, Optical control of selectivity of high rate CO$_2$ photoreduction via interband-or hot electron Z-scheme reaction pathways in Au-TiO$_2$ plasmonic photonic crystal photocatalyst, Appl. Catal. B 267 (2020) 118644.

[65] G. Almeida, L. Goldoni, Q. Akkerman, Z. Dang, A.H. Khan, S. Marras, I. Moreels, L. Manna, Role of acid–base equilibria in the size, shape, and phase control of cesium lead bromide nanocrystals, ACS Nano 12 (2018) 1704–1711.

[66] L. Hu, C. Wang, R.M. Kennedy, L.D. Marks, K.R. Poeppelmeier, The role of oleic acid: From synthesis to assembly of perovskite nanocuboid two-dimensional arrays, Inorg. Chem. 54 (3) (2015) 740–745.

[67] J. Xu, T. Chen, Q. Jiang, Y.-X. Li, Utilization of environmentally benign dicyandiamide as a precursor for the synthesis of ordered mesoporous carbon nitride and its application in base-catalyzed reactions, Chem. Asian J. 9 (11) (2014) 3269–3277.

[68] B. Lotsch, M. Döblinger, J. Sehnert, L. Seyfarth, J. Senker, O. Oeckler, W. Schnick, Unmasking melon by a complementary approach employing electron diffraction, solid-state NMR spectroscopy, and theoretical calculations—structural

characterization of a carbon nitride polymer, Chem. Eur. J. 13 (17) (2007) 4969–4980.

[69] X. Wang, K. Maeda, A. Thomas, K. Takanabe, G. Xin, J.M. Carlsson, K. Domen, M. Antonietti, A metal-free polymeric photocatalyst for hydrogen production from water under visible light, Nat. Mater. 8 (2009) 76.

[70] T.Y. Ma, Y. Tang, S. Dai, S.Z. Qiao, Proton-functionalized two-dimensional graphitic carbon nitride nanosheet: an excellent metal-/label-free biosensing platform, Small 10 (12) (2014) 2382–2389.

[71] Y. Kang, Y. Yang, L.C. Yin, X. Kang, L. Wang, G. Liu, H.M. Cheng, Selective breaking of hydrogen bonds of layered carbon nitride for visible light photocatalysis, Adv. Mater. 28 (2016) 6471–6477.

[72] W. Iqbal, B. Qiu, Q. Zhu, M. Xing, J. Zhang, Self-modified breaking hydrogen bonds to highly crystalline graphitic carbon nitrides nanosheets for drastically enhanced hydrogen production, Appl. Catal. B 232 (2018) 306–313.

[73] L. Lin, W. Ren, C. Wang, A. Asiri, J. Zhang, X. Wang, Crystalline carbon nitride semiconductors prepared at different temperatures for photocatalytic hydrogen production, Appl. Catal. B 231 (2018) 234–241.

[74] H. Ou, L. Lin, Y. Zheng, P. Yang, Y. Fang, X. Wang, Tri-s-triazine-based crystalline carbon nitride nanosheets for an improved hydrogen evolution, Adv. Mater. 29 (2017) 1700008.

[75] W. Xu, X. An, Q. Zhang, Z. Li, Q. Zhang, Z. Yao, X. Wang, S. Wang, J. Zheng, J. Zhang, W. Wu, M. Wu, Cesium salts as mild chemical scissors to trim carbon nitride for photocatalytic H_2 evolution, ACS Sust. Chem. Eng. (2019).

[76] T.S. Miller, T.M. Suter, A.M. Telford, L. Picco, O.D. Payton, F. Russell-Pavier, P. L. Cullen, A. Sella, M.S.P. Shaffer, J. Nelson, V. Tileli, P.F. McMillan, C. A. Howard, Single crystal, luminescent carbon nitride nanosheets formed by spontaneous dissolution, Nano Lett. 17 (10) (2017) 5891–5896.

[77] C. Ott, F. Reiter, M. Baumgartner, M. Pielmeier, A. Vogel, P. Walke, S. Burger, M. Ehrenreich, G. Kieslich, D. Daisenberger, J. Armstrong, U.K. Thakur, P. Kumar, S. Chen, D. Donadio, L.S. Walter, R.T. Weitz, K. Shankar, T. Nilges, Flexible and ultrasoft inorganic 1D semiconductor and heterostructure systems based on SnIP, Adv. Funct. Mater. 29 (18) (2019) 1900233.

[78] L. Lin, H. Ou, Y. Zhang, X. Wang, Tri-s-triazine-based crystalline graphitic carbon nitrides for highly efficient hydrogen evolution photocatalysis, ACS Catal. 6 (6) (2016) 3921–3931.

[79] A. Kumar, P. Kumar, C. Joshi, S. Ponnada, A.K. Pathak, A. Ali, B. Sreedhar, S. L. Jain, A $[Fe(bpy)_3]^{2+}$ grafted graphitic carbon nitride hybrid for visible light assisted oxidative coupling of benzylamines under mild reaction conditions, Green Chem. 18 (8) (2016) 2514–2521.

[80] G.P. Mane, S.N. Talapaneni, K.S. Lakhi, H. Ilbeygi, U. Ravon, K. Al-Bahily, T. Mori, D.-H. Park, A. Vinu, Highly ordered nitrogen-rich mesoporous carbon nitrides and their superior performance for sensing and photocatalytic hydrogen generation, Angew. Chem. Int. Ed. 56 (29) (2017) 8481–8485.

[81] D.M. Haiber, P.A. Crozier, Nanoscale probing of local hydrogen heterogeneity in disordered carbon nitrides with vibrational electron energy-loss spectroscopy, ACS Nano 12 (6) (2018) 5463–5472.

[82] N. Axén, G.A. Botton, R.E. Somekh, I.M. Hutchings, Effect of deposition conditions on the chemical bonding in sputtered carbon nitride films, Diam. Relat. Mater. 5 (2) (1996) 163–168.

[83] L.-C. Chen, C.-Y. Teng, C.-Y. Lin, H.-Y. Chang, S.-J. Chen, H. Teng, Architecting nitrogen functionalities on graphene oxide photocatalysts for boosting hydrogen production in water decomposition process, Adv. Energy Mater. 6 (22) (2016) 1600719.

[84] A. Kumar, P. Kumar, R. Borkar, A. Bansiwal, N. Labhsetwar, S.L. Jain, Metal-organic hybrid: photoreduction of CO_2 using graphitic carbon nitride supported heteroleptic iridium complex under visible light irradiation, Carbon 123 (2017) 371–379.

[85] Y.-Y. Li, B.-X. Zhou, H.-W. Zhang, S.-F. Ma, W.-Q. Huang, W. Peng, W. Hu, G.-F. Huang, Doping-induced enhancement of crystallinity in polymeric carbon nitride nanosheets to improve their visible-light photocatalytic activity, Nanoscale 11 (14) (2019) 6876–6885.

[86] P. Kumar, P. Kar, A.P. Manuel, S. Zeng, U.K. Thakur, K.M. Alam, Y. Zhang, R. Kisslinger, K. Cui, G.M. Bernard, Noble metal free, visible light driven photocatalysis using TiO_2 nanotube arrays sensitized by P-doped C_3N_4 quantum dots, Adv. Opt. Mater. (2019).

[87] L.u. Sun, M. Yang, J. Huang, D. Yu, W. Hong, X. Chen, Freestanding graphitic carbon nitride photonic crystals for enhanced photocatalysis, Adv. Funct. Mater. 26 (27) (2016) 4943–4950.

[88] G. Zhang, A. Savateev, Y. Zhao, L. Li, M. Antonietti, Advancing the n→ π* electron transition of carbon nitride nanotubes for H_2 photosynthesis, J. Mater. Chem. A 5 (25) (2017) 12723–12728.

[89] S. Guo, Y. Zhu, Y. Yan, Y. Min, J. Fan, Q. Xu, Holey structured graphitic carbon nitride thin sheets with edge oxygen doping via photo-Fenton reaction with enhanced photocatalytic activity, Appl. Catal. B 185 (2016) 315–321.

[90] J.K. Kim, S. Park, R.J. Yoo, H.J. Jeong, J. Oh, Y.J. Lee, S. Park, D.W. Kim, Thin PEGylated carbon nitrides: water-dispersible organic nanodots as bioimaging probes, Chem. Eur. J. 24 (14) (2018) 3506–3511.

[91] R. Yuan, L. Shen, C. Shen, J. Liu, L. Zhou, W. Xiang, X. Liang, CsPbBr $3:xEu^{3}+$ perovskite QD borosilicate glass: a new member of the luminescent material family, Chem. Commun. 54 (27) (2018) 3395–3398.

[92] J.Y. Woo, Y. Kim, J. Bae, T.G. Kim, J.W. Kim, D.C. Lee, S. Jeong, Highly stable cesium lead halide perovskite nanocrystals through in situ lead halide inorganic passivation, Chem. Mater. 29 (17) (2017) 7088–7092.

[93] V.K. Ravi, P.K. Santra, N. Joshi, J. Chugh, S.K. Singh, H. Rensmo, P. Ghosh, A. Nag, Origin of the substitution mechanism for the binding of organic ligands on the surface of CsPbBr 3 perovskite nanocubes, J. Phys. Chem. Lett. 8 (20) (2017) 4988–4994.

[94] J. Xu, L. Zhang, R. Shi, Y. Zhu, Chemical exfoliation of graphitic carbon nitride for efficient heterogeneous photocatalysis, J. Mater. Chem. A 1 (46) (2013) 14766–14772.

[95] X. Lu, K. Xu, P. Chen, K. Jia, S.i. Liu, C. Wu, Facile one step method realizing scalable production of gC$_3$N$_4$ nanosheets and study of their photocatalytic H_2 evolution activity, J. Mater. Chem. A 2 (44) (2014) 18924–18928.

[96] J. Jiang, L. Ou-yang, L. Zhu, A. Zheng, J. Zou, X. Yi, H. Tang, Dependence of electronic structure of g-C_3N_4 on the layer number of its nanosheets: a study by Raman spectroscopy coupled with first-principles calculations, Carbon 80 (2014) 213–221.

[97] R. Zhang, B. Li, J. Yang, Effects of stacking order, layer number and external electric field on electronic structures of few-layer $C_2N–h_2D$, Nanoscale 7 (33) (2015) 14062–14070.

[98] J.-H. Cha, J.H. Han, W. Yin, C. Park, Y. Park, T.K. Ahn, J.H. Cho, D.-Y. Jung, Photoresponse of CsPbBr 3 and C$_s$4PbB$_r$6 perovskite single crystals, J. Phys. Chem. Lett. 8 (3) (2017) 565–570.

[99] A.M. Askar, K. Shankar, Exciton binding energy in organic–inorganic tri-halide perovskites, J. Nanosci. Nanotechnol. 16 (6) (2016) 5890–5901.

[100] Y. Zhang, Q. Pan, G. Chai, M. Liang, G. Dong, Q. Zhang, J. Qiu, Synthesis and luminescence mechanism of multicolor-emitting gc$_3$N$_4$ nanopowders by low temperature thermal condensation of melamine, Sci. Rep. 3 (2013) 1943.

[101] Y. Guo, J. Li, Y. Yuan, L.u. Li, M. Zhang, C. Zhou, Z. Lin, A Rapid microwave-assisted thermolysis route to highly crystalline carbon nitrides for efficient hydrogen generation, Angew. Chem. Int. Ed. 55 (47) (2016) 14693–14697.

[102] P. Xia, B. Zhu, J. Yu, S. Cao, M. Jaroniec, Ultra-thin nanosheet assemblies of graphitic carbon nitride for enhanced photocatalytic CO_2 reduction, J. Mater. Chem. A 5 (7) (2017) 3230–3238.

[103] R. Godin, Y. Wang, M.A. Zwijnenburg, J. Tang, J.R. Durrant, Time-resolved spectroscopic investigation of charge trapping in carbon nitrides photocatalysts for hydrogen generation, J. Am. Chem. Soc. 139 (14) (2017) 5216–5224.

[104] M.Z. Rahman, J. Ran, Y. Tang, M. Jaroniec, S.Z. Qiao, Surface activated carbon nitride nanosheets with optimized electro-optical properties for highly efficient photocatalytic hydrogen production, J. Mater. Chem. A 4 (7) (2016) 2445–2452.

[105] Q. Wang, L. Tao, X. Jiang, M. Wang, Y. Shen, Graphene oxide wrapped CH$_3$NH$_3$PbBr 3 perovskite quantum dots hybrid for photoelectrochemical C$_O$2 reduction in organic solvents, Appl. Surf. Sci. 465 (2019) 607–613.

[106] Q. Wang, S. Yu, W. Qin, X. Wu, Isopropanol-assisted synthesis of highly stable MAPbBr 3/pg$_C$3N4 intergrowth composite photocatalysts and their interfacial charge carrier dynamics, Nanoscale Adv. 2 (1) (2020) 274–285.

[107] M. Ou, W. Tu, S. Yin, W. Xing, S. Wu, H. Wang, S. Wan, Q. Zhong, R. Xu, Amino-assisted anchoring of CsPbBr 3 perovskite quantum dots on porous g-c$_3$N4 for enhanced photocatalytic C$_O$2 reduction, Angew. Chem. 130 (2018) 13758–13762.

[108] D. Cruz, J. Garcia Cerrillo, B. Kumru, N. Li, J. Dario Perea, B.V. Schmidt, I. Lauermann, C.J. Brabec, M. Antonietti, Influence of Thiazole-modified carbon nitride nanosheets with feasible electronic properties on inverted perovskite solar cells, J. Am. Chem. Soc. 141 (2019) 12322–12328.

[109] Z. Tian, S. Wang, Y. Wang, X. Ma, K. Cao, D. Peng, X. Wu, H. Wu, Z. Jiang, Enhanced gas separation performance of mixed matrix membranes from graphitic carbon nitride nanosheets and polymers of intrinsic microporosity, J. Membr. Sci. 514 (2016) 15–24.

[110] J. Ran, T. Pan, Y. Wu, C. Chu, P. Cui, P. Zhang, X. Ai, C. Fu, Z. Yang, T. Xu, Endowing g-C$_3$N$_4$ membranes with superior permeability and stability by using acid spacers, Angew. Chem. Int. Ed. 58 (2019) 16463–16468.

[111] H. Du, J. Li, J. Zhang, G. Su, X. Li, Y. Zhao, Separation of hydrogen and nitrogen gases with porous graphene membrane, J. Phys. Chem. C 115 (2011) 23261–23266.

[112] D.H. Park, K.S. Lakhi, K. Ramadass, M.K. Kim, S.N. Talapaneni, S. Joseph, U. Ravon, K. Al-Bahily, A. Vinu, Energy efficient synthesis of ordered mesoporous carbon nitrides with a high nitrogen content and enhanced CO_2 capture capacity, Chem. Eur. J. 23 (2017) 10753–10757.

[113] F. Goettmann, A. Thomas, M. Antonietti, Metal-free activation of CO_2 by mesoporous graphitic carbon nitride, Angew. Chem. Int. Ed. 46 (2007) 2717–2720.

[114] W. Ren, J. Cheng, H. Ou, C. Huang, M.-M. Titirici, X. Wang, Enhancing visible-light hydrogen evolution performance of crystalline carbon nitride by defect engineering, ChemSusChem 12 (14) (2019) 3257–3262.

[115] P. Yang, H. Ou, Y. Fang, X. Wang, A facile steam reforming strategy to delaminate layered carbon nitride semiconductors for photoredox catalysis, Angew. Chem. Int. Ed. 56 (2017) 3992–3996.